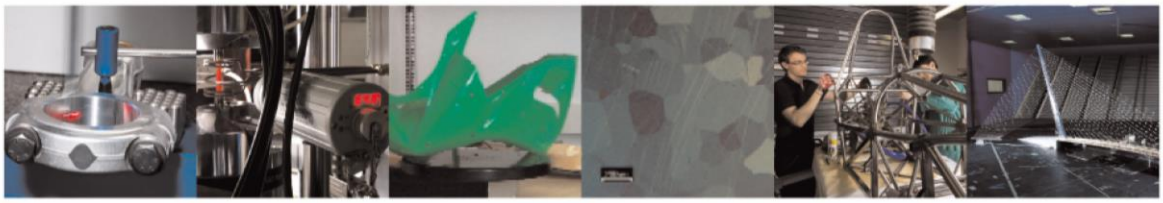

Additively manufactured Fe-35Mn-1Ag lattice structures for biomedical applications

A. Dehghan-Manshadi, J. Venezuela, A.G. Demir, Q. Ye, M.S. Dargusch

This is a post-peer-review, pre-copyedit version of an article published in Journal of Manufacturing Processes. The final authenticated version is available online at: http://dx.doi.org/10.1016/j.jmapro.2022.06.010

Additively manufactured Fe-35Mn-1Ag lattice structures for biomedical applications

A. Dehghan-Manshadi[a], J. Venezuela[a], A.G. Demir[b], Q. Ye[c] and M. S. Dargusch[a,*],

[a] Queensland Centre for Advanced Materials Processing and Manufacturing (AMPAM) School of Mechanical and Mining Engineering, The University of Queensland, St Lucia, QLD 4072, Australia

[c] Department of Mechanical Engineering, Politecnico di Milano, Via La Masa 1, 20156, Milan, Italy

[d] Centre of Regenerative Medicine, Renmin Hospital of Wuhan University, Wuhan University, Wuhan, Wuhan, 430060, China

[*] Corresponding authors Email: m.dargusch@uq.edu.au

Keywords: Additive Manufacturing; SLM; Biomaterials; Mechanical Properties; Biodegradation; Fe-Mn-Ag Alloy

Abstract

Highly porous scaffolds of Fe-35Mn-1Ag biodegradable alloy fabricated for the first time using the selective laser melting technique. The microstructure, structural morphology, mechanical properties and degradation behaviour of the scaffold were studied and the results compared with a Fe-35Mn scaffold manufactured under similar processing parameters. The SLM fabricated scaffold exhibits a well-developed pore structure with high levels of interconnectivity, promoting improved biocompatibility. The mechanical properties are very close to those of the target human tissue promising no stress shielding after implantation. While, Fe-35Mn-1Ag scaffold shows slightly higher mechanical properties compared with Fe-35Mn alloy, the degradation rate increased by more than 30%. Overall, the SLM fabricated Fe-35Mn-1Ag scaffolds exhibited promising mechanical properties along with improved degradation behaviour, offering a solution for biodegradable load bearing applications.

1) Introduction

Biodegradable implants are increasingly used in various fields such as cardiology, orthopaedic surgery, general surgery, maxillofacial surgery, gynaecology, and urology [1]. Among all biodegradable materials, metals are an excellent choice due to their biocompatibility, high mechanical properties and ease of manufacturing. More importantly, metals can offer the opportunity to tailor their physical and mechanical properties as well as biodegradation rate, to meet the requirement for any specific implant application. Such adjustments in the properties of metallic implants can be achieved through altering the chemical composition, geometrical design, manufacturing technique or composite with non-metallic materials [2-4]. Traditionally, metallic implants made from stainless steel, titanium alloy, tantalum, nitinol (Ni and Ti alloy) and cobalt-chromium alloys [5, 6], which remain in the body permanently or need to be

removed after certain time by secondary surgery. Over time, such permanent implants can cause different problems such as stress shielding (a mechanical mismatch between implant and surrounding bone) [7], release of toxic metal ions such as Ni [8] and discomfort of a foreign object in the patient body. Therefore, application of biodegradable implants, which are able to dissolve in the body fluid stream after certain service time, can overcome most of the aforementioned complications with permanent implants.

Different metals such as magnesium (Mg), iron (Fe), and zinc (Zn) are attractive biomaterials with degradation behaviour. While, Mg based alloys are the most common biodegradable metallic implants with clinical approvals (such as stents application [9]), they suffer from some important limitations [10, 11]. These include i) high degradation rate which may cause rapid decrease in the mechanical/functional integrity, ii) low mechanical properties for load bearing applications and iii) release of H_2 gas bubbles as a result of Mg chemical reaction [10-14]. Compared with Mg, iron and its alloys are attractive biodegradable materials for implants with superior mechanical properties, excellent biocompatibility and degradability in the human body environment [5, 11, 15]. However, some challenges remain with the clinical application of Fe as a biodegradable implant. These challenges are related to the slow degradation rate of Fe as well as its non-compatibility with magnetic resonance imaging (MRI) [11]. Recently, many research and clinical activities focussed on the improvement of biodegradability of Fe through alloying with either active elements such as Mn [1, 11, 16-26], Si [27, 28], Cu [29], Al [20], W [30] or noble metals (Pd [31] and Ag [5, 32-34]). Micro-alloying with biocompatible elements such as Mo, also offered a new potential for biodegradable Fe-based alloys [35]. While active elements facilitate the degradation of Fe by reducing the standard electrode potential of the Fe matrix, the noble elements promote galvanic corrosion by forming intermetallic particles [36]. For instance, different compositions of Fe-Mn alloys have been proposed as biodegradable implants due to their accelerated degradation (compared with pure Fe), enhanced mechanical properties (for load bearing applications) and magnetic resonance imaging compatibility [5, 11, 17, 21, 22, 25, 37]. The current authors have performed comprehensive research on in vitro and in vivo behaviour of Fe-Mn [11, 18] alloys as promising biodegradable Fe based implants. These results suggests that Fe-35Mn can offer the best combination of mechanical properties and degradation rate [11].

While the Fe-35Mn alloy demonstrated its good biocompatibility, the degradation rate of this alloy is still far from the ideal rate for load bearing applications [36]. Therefore, further improvement in the alloy composition, structural design and fabrication technique are required to increase the biodegradability. In this regards, the current authors have suggested that small additions of Ag to the Fe-35Mn composition significantly increased its degradation rate [5]. While Fe-35Mn alloy showed a degradation rate of 0.31 mm/year under standard immersion tests, addition of 1.0 wt% silver increased the degradation rate to 0.88 mm/year [5]. Similar results have also been reported for other Fe-Mn alloys. For instance, Liu et al [34], reported a 70% increase in the degradation rate of Fe-30Mn alloy by small addition of Ag. They proposed that such corrosion rate enhancement could be due to the precipitation of Ag-rich particles on the Fe-Mn grain boundaries. Similarly, Sotudehbagha et al [33], reported an accelerated degradation rate in a nano-structured Fe-30Mn-(1-3)Ag alloys manufactured by metal alloying processes.

It is worth noting that an additional benefit of alloying with Ag correspond to its antibacterial effect. Research and clinical investigation suggests that, despite considerable improvement in the invasive surgery as well as aseptic techniques, the implant related infections remain the biggest challenge for implantation surgery. It has been shown [38] that even advanced antibiotics and their systematic usage are ineffective in preventing implant infections manly due to the antibiotic resistance of bacteria, insufficient drug penetration and no optimal availability of used antibiotics in the implanted sites [38, 39]. Therefore, integrating the antibacterial medicine (especially metallic ions with antibacterial properties such as Ag, Cu, Li and Zn) into the implant structure and in the form of additives or coating before implantation process, would be more effective as implanted materials can provide antibacterial drugs directly into the implanted area preventing any infection [40-43]. It has been shown that Ag ions have higher antibacterial activity compared to Cu or Zn [38, 40, 41, 44] and Ag is able to kill bacteria through generation of reactive oxygen species (ROS) [44]. Therefore, while addition of Ag to the Fe-Mn biomedical alloys can accelerates its degradation rate and improve its mechanical properties, Ag can enhance the biocompatibility of the alloy through introducing antibacterial properties to the implant.

To this point, as suggested in previous work [5], the Fe-35Mn-1Ag alloy offers an improved biocompatibility with enhanced degradation rate, suitable for many biomedical applications. However, previous work limits the fabrication of samples to the traditional manufacturing technique of powder metallurgy. Such traditional techniques usually have limitations on design and manufacturing of highly porous structures, which are essential for implant design. In fact, despite acceptable degradation rate and mechanical properties, an ideal implant (especially bone scaffold) needs to have an internal porous structure with good pore interconnectivity to allow tissue regeneration and direct bonding to the natural tissue [11, 45]. Therefore, using an advanced manufacturing technique provides capability for fabrication of implants with controlled and interconnected pore structures and complex geometry. Therefore, additive manufacturing (AM) techniques are able to increase the biocompatibility of the implant and tailor the mechanical properties according to the requirements for any specific implant application.

Selective laser melting (SLM) is an emerging advanced manufacturing technique offering solutions to the fabrication of highly complex components such as biomedical implants and devices [1, 46]. This process uses a laser beam to melt metal powder in a layer-by-layer fashion to build components from their 3D CAD models, as shown in Figure 1. SLM allows design and manufacturing of implants with complex and net shape geometries with high porosity and interconnected pores [47, 48]. Most importantly, SLM is able to tailor the mechanical, physical and biomedical properties of implants through controlling the internal porosity, density and chemical composition of manufactured implants. For instance, SLM is able to produce complex porous structures with densities ranging from 100% (full density) to as little as 2.0% [49]. Moreover the fast cooling cycles of SLM induce a refined microstructure enhancing the mechanical and corrosion properties of the biodegradable alloys [50]. SLM is an established process when using well established-alloyed powders, although the biodegradable alloys pose different challenges to process-ability. The manufacturing of metallic implants with different compositions through elemental mixing is possible, however, it requires further attention in

terms of the process-ability [51]. Also, SLM give the opportunity (through controlled geometry and architecture) to design metallic scaffolds with different functionalities and properties for biomedical applications [48]. This requires tailoring the architectural features, pore shape and size without altering the mechanical performance of the scaffolds [48]. The design of scaffolds may be even further improved by programmatically changing the shape and function of additively manufactured scaffolds over time (the concept of 4D) [52]. Therefore, SLM offer a unique opportunity to fabricate Fe-35Mn porous implants with a controlled addition of Ag or other elements with metallurgical compatibility. Indeed the high reflectivity of Ag present in the mixed powder feedstock is a challenging point to be addressed [53]. In addition, this should be noted that despite unique advantages of SLM for manufacturing of biodegradable implants, there are some limitations as well. These limitations, which mostly related to the low melting point and high vapour pressure of biodegradable metals, are more severe for common biodegradable metals such as Mg and Zn. However, presence of Mn with high vapour pressure could add some complication to the SLM manufacturing of implants in the current study. Such complications minimised by using pre-alloyed Fe-Mn powder in the feedstock.

In this work, the physical, mechanical and degradation behaviour of Fe-35Mn-1Ag scaffolds fabricated through selective laser melting process were investigated and the results compared with Fe-35Mn alloy as the reference material. To the best of our knowledge, this study is the first report on fabrication of highly porous Fe-35Mn-1Ag biomedical alloy using the SLM technique.

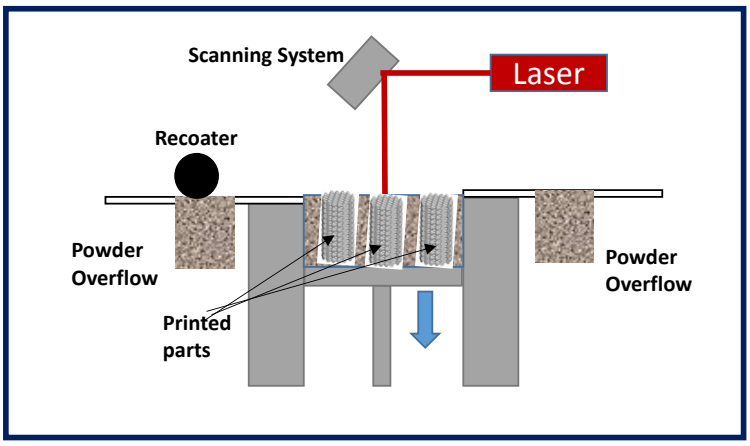

Figure 1 Schematic diagram representing SLM process

2) Materials and Methods

2-1) Materials:

Pre-alloyed spherical gas atomised powder of Fe-35Mn alloy (supplied by Höganäs AB, Sweden) with the nominal composition of (wt%) Mn: 34.70, C: 0.07, S: 0.006, and balance Fe, and particle size of <45µm were used as initial powder. Silver powders of 99.9% purity and 5-8 µm size also supplied by Sigma Aldrich. For feedstock preparation, the correct weight of Fe-35Mn and Ag powders mixed in a 3D Turbula mixer for 6 hours.

2-2) SLM Process

Selective laser melting of both Fe-35Mn and Fe-35Mn-1Ag scaffolds carried out using an industrial SLM Solutions 125 HL machine equipped with a 400 W IPG fibre laser. The laser spot diameter and wavelength was 80 μm and 1070nm, respectively. The SLM parameters for both Fe-35Mn and Fe-35Mn-1Ag lattices were the same. Laser power was set at 150 W, layer thickness was 30 μm, scanning speed was chosen as 640 mm/s and hatch spacing was 0.096 mm. These values selected as optimum parameters based on the previous studies [1, 46] and preliminary experiments, which are not reported for brevity. All the builds were performed under a "chessboard" scanning strategy. In addition, the substrate plate was pre heated to 200 °C prior to the start of printing. No upskin, downskin or border parameter sets were employed.

Schwarz Primitive Surface p-unit has been used for the lattice structure design, as these unit cells have shown excellent fluid permeability, stress distribution and high stress to weight ratio [1, 54], all are essential for bone scaffold. The scaffolds were designed to have an overall density of 60%, pore size of 500 μm and maximum strut of 700 μm on printed samples.

2-3) Materials Characterization

The surface of as-build scaffolds studied using Hitachi TM3030 tabletop Scanning Electron Microscopy (SEM). The cross section of the printed samples also studied using optical and electron microscopy after standard metallographic preparation and etching in 2.0% Nital solution.

The processed structure, surface area and porosity of manufactured samples measured using Micro-CT scan and dry weight. Micro-CT studies were performed using a preclinical Inveon micro-computed tomography (μCT) scanner (Siemens, Berlin Germany) under 80 kV voltage, 150 μA current, 4000 ms exposure size and scanning resolution of 16 μm. The images of scanned samples were reconstructed using a Feldkamp reconstruction software (Siemens). The porosity (ρ) measured using dry weigh of samples and following formula [46]:

$$\rho(\%) = (1 - \frac{M_{air}}{M_{ideal}}) \times 100 \qquad (1)$$

Where ρ is the porosity (%), M_{air} is the dry mass of sample in air and M_{ideal} is the theoretical mass of solid sample of the similar material with similar dimensions.

As expected from any SLM manufactured sample, some micron size porosity remain within the solid part of the structure (internal porosity), which could affect final density of samples. The internal porosity was measured using microstructural studies.

Compression tests were performed using an Instron 5584 machine under a cross head movement rate of 1×10^{-3} mm/s. The constituent phases of the sintered samples were evaluated by X-Ray diffraction (XRD) using the Bruker D8 Advance MKII XRD diffractometer operated at 40 kV and 40 mA with Cu Kα radiation (λ = 0.15406 nm). The scanning angle of 20-100° and the scan rate of 2°/min applied.

2-4) Immersion Testing:

In order to evaluate the degradation behaviour of samples, immersion testing was performed for 28 days in Hank's balanced solution (Sigma H1387: 8.0 g sodium chloride (NaCl), 0.14 g calcium chloride ($CaCl_2$), 0.4 g potassium chloride (KCl), 0.35 g sodium bicarbonate ($NaHCO_3$), 1.0 g glucose, 0.048 g sodium phosphate dibasic (Na_2HPO_4, anhydrous), 0.06 g potassium dihydrogen phosphate (KH_2PO_4, anhydrous), 0.097 g magnesium sulfate ($MgSO_4$, anhydrous). During the test, the solution temperature and pH were maintained at 37 ± 2°C and 7.4 ± 0.2, respectively. To keep the PH constant, the solution changed with fresh one every 48 hours. Test samples were SLM manufactured cylinders with ø6 mm ×12 mm dimension. Prior to immersion testing, the samples were ultrasonically cleaned in ethanol for 5 min, rinsed in distilled water and blow-dried. The weight and dimension of samples were measured and recorded before the immersion test. A minimum of three specimens were tested for each alloy type.

At the end of 28 days, the specimens were taken out, and the corrosion products were cleaned using a solution of phosphoric and citric acid. The corrosion rate was calculated using:

$$CR_i = 8.71 \times 10^4 \frac{w}{At\rho} \qquad [1]$$

where W is the weight loss, A is the exposure area as measured from the micro-CT scan images, t is the time of exposure and ρ is the density of the printed samples measured using Archimedes technique. The microstructure of the samples was investigated under SEM before the immersion test, after immersion (pre-cleaning), and after corrosion cleaning.

3) Results and Discussion:

3-1) Powder characterization

Figure 2 shows the morphology of the Fe-35Mn, Ag as well as mixed Fe-35Mn-1Ag powders. It is clear that the Fe-35Mn powder has a spherical morphology with particle size ranging from 0-45 μm. The EDS spectrum and quantitative analysis of powder show strong peaks of Fe and Mn (Figure 2d) and the composition very close to the nominal value of 65wt% Fe and 35wt% Mn, indication of high purity of Fe-35Mn initial powder. In comparison, the SEM image of silver powder show very fine, irregular shape and agglomerated particles of Ag (Figure 2b). The morphology and distribution of Fe-35Mn-1Ag mixed powder (SLM feedstock) shown in Figure 2c along with EDS map of Fe, Mn and Ag elements (Figure 2e). After the mixing procedure, the Ag agglomeration appears to be reduced to a certain extent. The Fe-35Mn and Ag particles remain separate without the presence of penetration of one into the other in a mechanical alloying manner. While Ag particles are homogeneously distributed within the Fe-35Mn powder, some agglomeration of Ag particles remains visible in the selected area due to the very fine particle size of Ag. The presence of such agglomerated areas of Ag powder, can be expected to create some variations in the laser process-ability in the powder bed and non-homogeneity in the microstructure of the final SLM manufactured components.

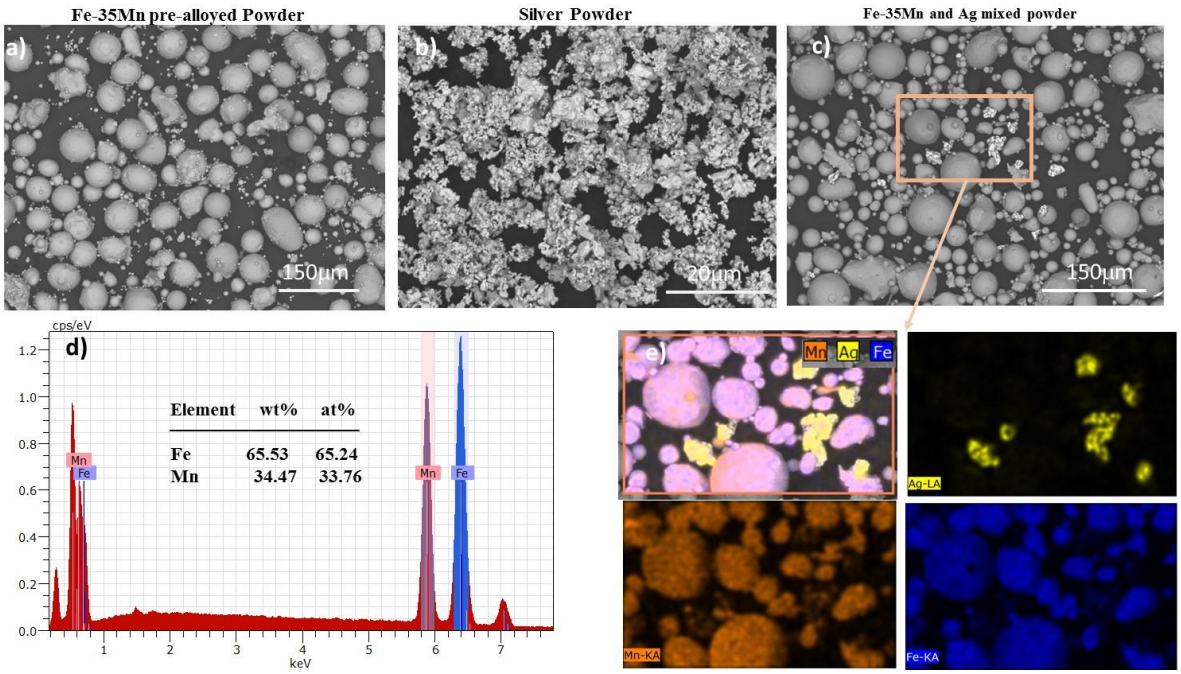

Figure 2 SEM micrograph of a) Fe-35Mn powder, b) Ag powder, c) Fe-35Mn-1Ag SLM feedstock. d) EDS spectrum of Fe-35Mn initial powder and e) EDS Map of Mn, Fe and Ag from SLM feedstock

3-2) Morphology and microstructure of SLM produced scaffolds

Figures 3a and 3b represents the as-designed model and as-built scaffolds, indicating a good agreement between geometry and morphology of designed and built samples. The as-built surface morphology of both Fe-35Mn and Fe-35Mn-1Ag scaffolds obtained by SEM is presented in Figures 3c and 3d, respectively. These SEM images indicate a uniform pore structure for both samples, representing suitability of applied SLM processing parameters. A slice from µCT scanning of an as-build Fe-35Mn-1Ag sample is also represented in Figure 3e to evaluate the internal structure of fabricated scaffolds.

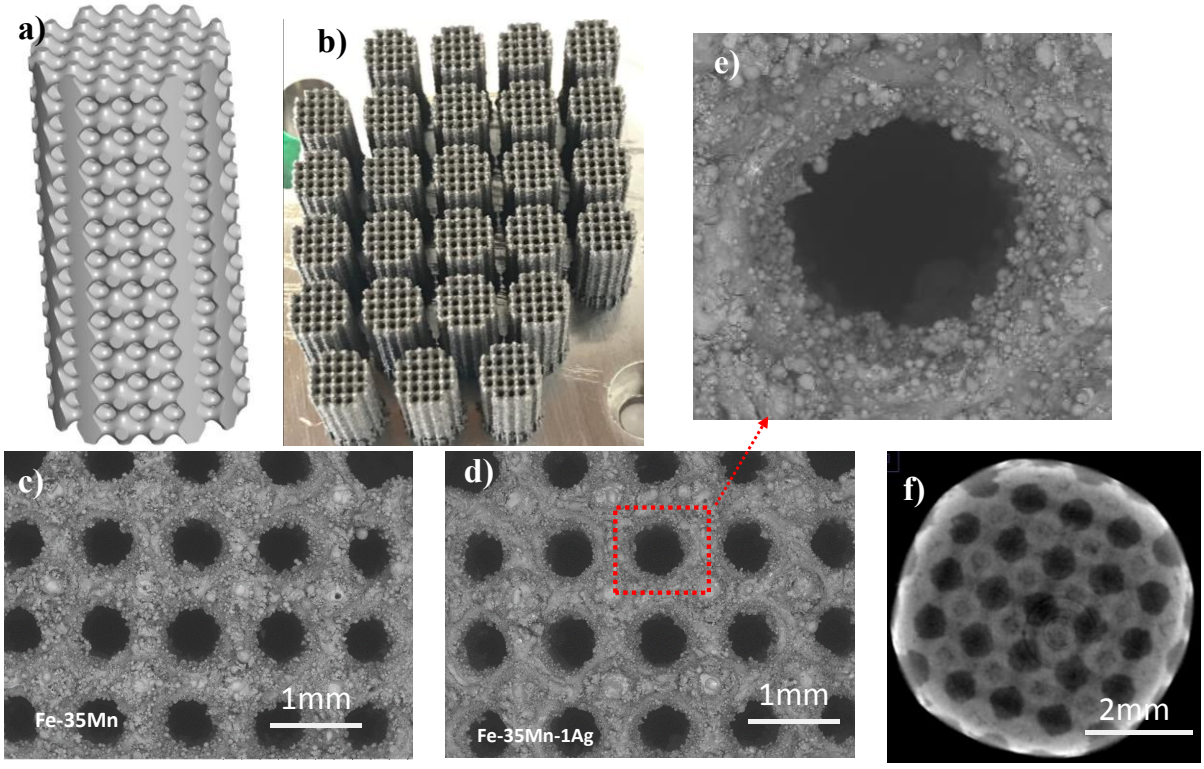

Figure 3 a) CAD model and b) as manufactured scaffolds, SEM image from surface morphology of as build scaffolds of c) Fe-35Mn and d) Fe-35Mn-aAg, e) high resolution SEM of surface morphology showing partially melted powders and melt pool extension structure, f) µ-Ct scan from internal structure of Fe-35Mn-1Ag scaffold

To evaluate the correlation between as-designed and as-built scaffolds, different parameters of scaffolds obtained from either SEM, µCT images and density measurements, are summarized in Table 1. Results show that both Fe-35Mn and Fe-35Mn-1Ag printed scaffolds have sufficient geometrical fidelity. However, addition of 1.0 wt% silver to the alloy creates some deviation in both internal porosity fraction (porosity of the matrix) and lattice porosity compared with Fe-35Mn alloy, but less influence on the surface area of scaffolds. While Fe-35Mn scaffolds shows only 0.63% internal porosity thorough its microstructural analysis, addition of Ag increased the porosity to 1.35%. The irregular pore shapes seen in Figure 3e indicate local lack-of-fusion defects. The optical absorptivity of Fe, Mn, and Ag [55, 56] to the non-polarized 1070 nm laser wavelength are 38%, 34%, and 0.3% respectively. For Fe-35Mn, the absorptivity of low-C steels at 35% can also be considered. On the other hand the melting temperatures of Fe-35Mn and Ag are 1387°C and 960°C respectively [57]. It can be deduced that the start difference between the optical absorptivity of the two powder types is compensated partially by the lower melting point of Ag. With the correct dispersion of smaller Ag particles in the Fe-35Mn powder, the process is observed to remain relatively stable. The melting of the Ag particles and consecutive mixing with the Fe-35Mn alloy can be expected to occur mainly due to the heat conduction from the molten pool rather than a direct absorption of the laser beam. With local increase in Ag fraction, the process may remain insufficiently energetic, generating the lack-of-fusion pores. An increase of Ag fraction in the Fe-35Mn powder may therefore further reduce the process-ability. On the other hand, the limited appearance of such pores within the thin struts indicate that the material is process-able and a

pre-alloyed Fe-35Mn-1Ag powder can potentially be more beneficial for defect-free porous structures.

However, there are big deviations from design to fabrication for both lattice porosity and surface area (Table 1). The biggest deviation relates to the lattice porosity of scaffolds, where the value of porosity declined from 60% in the designed model to 52% in Fe-35Mn and 53% in Fe-35Mn-1Ag fabricated samples. Such a large deviation previously reported for different SLM manufactured materials [58, 59] and mostly associated with the existence of excess powder trapped within the internal pores , adhesion of partially melted powders to the inner and outer surfaces and melt pool extension [58], which forms due to the lack of support in the substrate [59, 60]. Such defects in the SLM fabricated samples can cause surface roughness and, therefore, reduce the actual pore size and porosity of SLM fabricated structures. Surface topography of the produced scaffolds composed of partially melted powders and melt droplets can be observed from SEM images in Figures 3 d and e. The correct setting of the beam compensation parameter would be useful to improve the geometrical deviations due to the melt pool extension, while the sintered particles and melt droplets require successive post-processing methods to improve the surface quality [61].

Table 1 comparison between as designed and as-build values for lattice porosity, internal porosity (porosity of scaffold matrix) and surface area

	Material	As-Designed	As-Build
Lattice Porosity, %	Fe-35Mn-1Ag	60	52
	Fe-35Mn	60	53
Internal Porosity, %	Fe-35Mn-1Ag	0	1.35±0.09
	Fe-35Mn	0	0.63±0.06
Surface Area/Volume ratio	Fe-35Mn-1Ag	6.2	8.94±0.12
	Fe-35Mn	6.2	8.92±0.11

The surface roughness of the SLM fabricated samples also created a large deviation in the actual surface area (measured through analysis of μCT scanned images) compared with the model data. As seen in Table 1, the actual surface area/volume ratio increased from 6.2 in designed scaffolds to 8.94 and 8.92 in Fe-35Mn-1Ag and Fe-35Mn scaffolds, respectively. Such an increase in the surface area could affect the corrosion and degradation rate of scaffolds as increase the area of material in contact with the corrosive environment.

To further evaluate the effect of silver additions on the microstructural characteristics of SLM fabricated scaffolds, the microstructure of samples were studied using both optical and electron microscopes. Figure 4 shows typical microstructures of Fe-35Mn and Fe-35Mn-1Ag samples. The microstructure of Fe-35Mn sample (Figure 4a) predominantly consists of some large columnar austenite grains, indication of melting pool formation during SLM process. Detailed SEM images (later shown in Figure 5), indicated that these large columnar austenite grains consists a network of small and micron-size cell structure. As previously reported by Carluccio et al [1, 46], formation of such cellular solidification structure is dominant to the dendrite

formation under SLM processing conditions (i.e high cooling rate). The size of such columnar grains was reduced in Fe-35Mn-1Ag structures (Figure 4b).

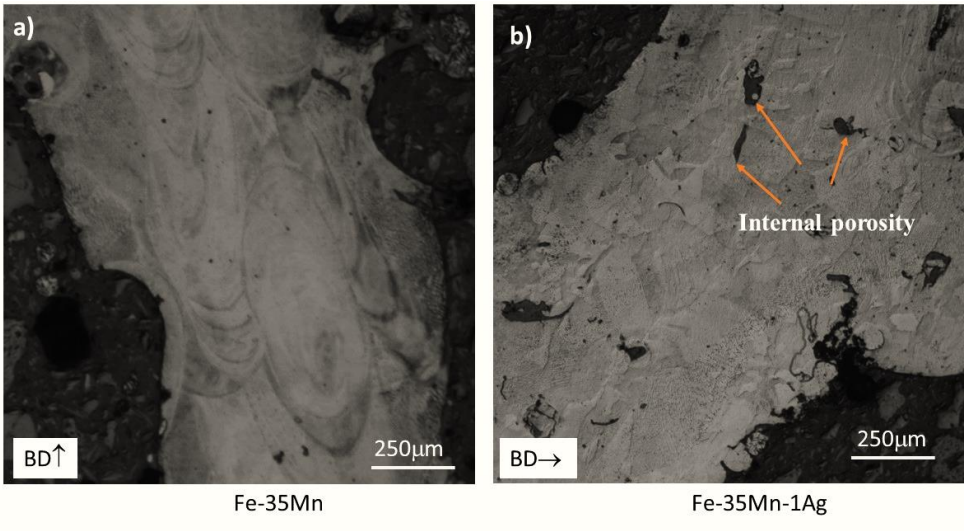

Figure 4 Optical microstructure from cross section of a) Fe-35Mn and b) Fe-35Mn-1Ag scaffolds

In general, a limited number of pores or cracks were observed in the matrix of the scaffolds. The volume fraction of pores was calculated from microstructural analysis and the results are reported in Table 1. However, Figure 4b reveals that the addition of Ag to the Fe-35Mn powder introduced some small porosity within the matrix (arrows in Figure 4). The presence of such internal porosity within the matrix of Fe-35Mn-1Ag samples is consistent with the density measurement data in Table 1. Figure 5 shows the detailed SEM images of both Fe-35Mn and Fe-35Mn-1Ag scaffolds. This figure indicates that the microstructure of both samples have a mixed morphology of equiaxed grains and columnar dendrites, which may have been formed due to the rapid cooling of the melted powder during the SLM process. Some micron-size pores are other features, which are visible in both microstructures (arrows in Figure 5). The presence of small porosity in the SLM manufactured samples is commonly reported in different materials [62-64].

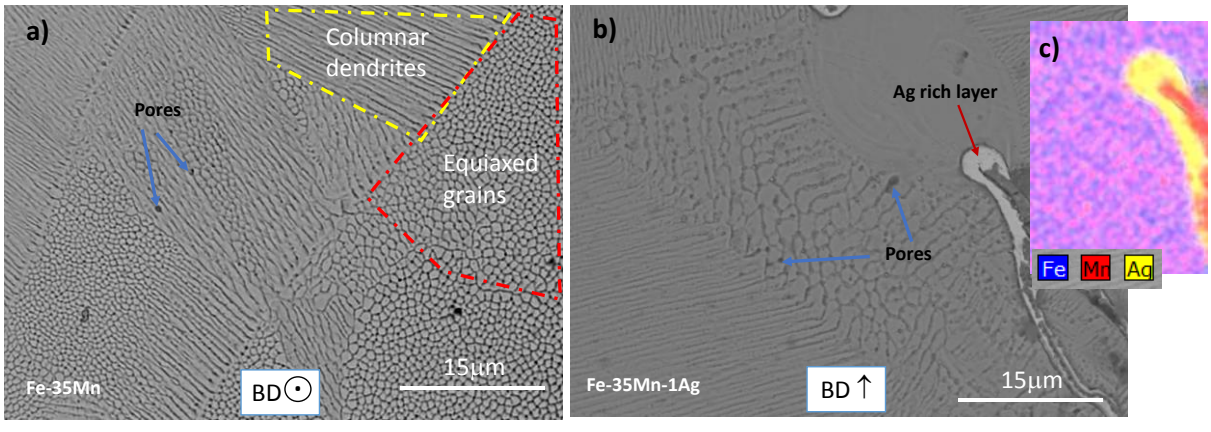

Figure 5 SEM micrograph from matrix of a) Fe-35Mn and b) Fe-35Mn1ag scaffolds. Arrows show the micron-size pores within both structures, c) EDS map from Ag-rich area in Fe-35Mn-1Ag scaffold

As seen in Figure 5b, in some areas of the Ag added sample, a large and elongated layer of Ag-rich is visible. This could be due to the agglomeration of Ag particles in SLM feedstock (as

seen in Figure 2c). As silver melting point (960 °C) is lower than Fe-35Mn alloy (1382°C), the Ag particles will fully melted during the laser scanning, diffuse around the Fe-Mn grain boundaries, and form Ag-rich layer. Such layer can even re-melt during the scanning and printing of next layer/s, extend its diffusion within the matrix grain boundaries, and form such elongated Ag-rich layer. The observations of large Ag-rich particles/layers are consistent with previous works where Fe-Mn-Ag scaffolds manufacture either by powder metallurgy [5], mechanical alloying [33] or casting processes [34].

The XRD spectra of SLM manufactured scaffolds have been represented in Figure 6. As expected for a Fe-alloy with high Mn content (higher than 27 wt% [65]), the major constituent phase for both samples is Face-Centred-Cubic (FCC) γ-Austenite. However, small peaks of Hexagonal-Close-pack (HCP) ε-martensite phase were also observed, which could be due to the rapid cooling characteristics of the SLM process. Figure 6 reveals that while the intensity of all austenite peaks are slightly stronger in Fe-35Mn alloy; those of the martensite phase are stronger for the Fe-35Mn-Ag alloy, indicating higher volume fraction of martensite phase in the later alloy. As previously stated and confirmed by SEM images (Figure 5), small precipitates of Ag-rich alloy formed within the matrix of Fe-35Mn-Ag alloy. Such Ag-rich particles could promote martensite formation during rapid cooling of Fe-Mn alloy in SLM process.

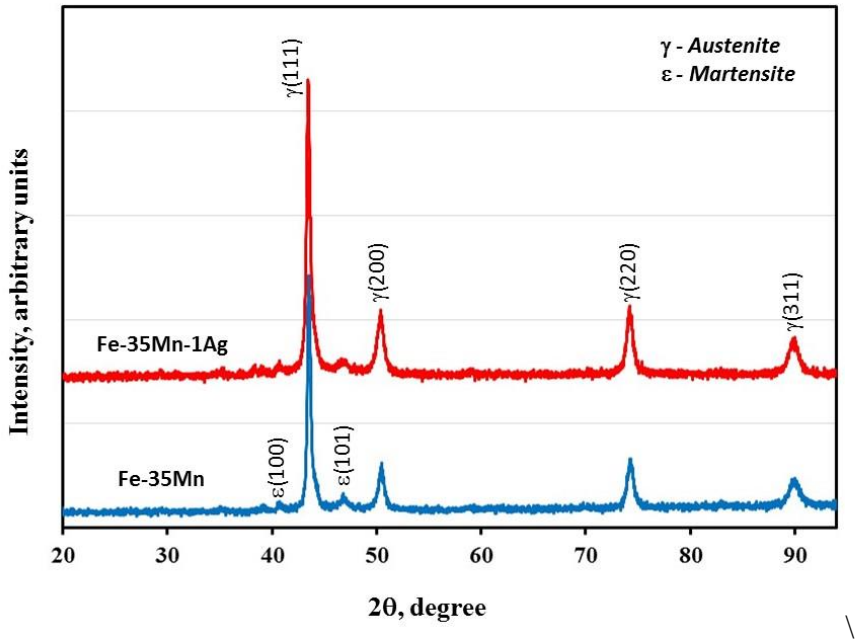

Figure 6 XRD spectra of Fe-35Mn and Fe-35Mn-1ag scaffolds showing strong peaks of Austenite phase in both alloy

3-3) Mechanical properties

The mechanical properties of SLM fabricated Fe-35Mn and Fe-35Mn-1Ag porous scaffolds were investigated using standard compression testing. Figure 7 shows the typical compression test curves for both Fe-35Mn and Fe-35mn-1Ag scaffolds. The corresponding mechanical properties (stress at 0.2%, $\sigma_{0.2}$, stress at 30%, σ_{30} and Young's Modulus, E_c) along with the comparable properties for human cortical bone [66] have been reported in Table 2. The

mechanical properties represented in this table indicate that both Fe-35Mn and Fe-35Mn-1Ag scaffolds manufactured by SLM are well suited with an acceptable level of mechanical properties for biomedical implant engineering. However, additions of silver enhanced the mechanical properties. As seen, the compressive strength of SLM manufactured Fe-35Mn scaffold with 60% porosity reached to a value of 235 MPa but increased to 324 MPa when 1.0 wt% silver added to the composition. Such an increase in the strength of the Fe-35Mn-1Ag could be attributed to the effect of Ag on grain refinement of the Fe-35Mn matrix (as seen in Figure 4) together with precipitation of Ag-rich particles on the grain boundaries [5, 34]. Table 2 also demonstrates that the Young's modulus of both scaffolds are very similar to the recommended value for human bone, which could prevent any stress shielding when used as a load bearing bone scaffolds in the human body [7].

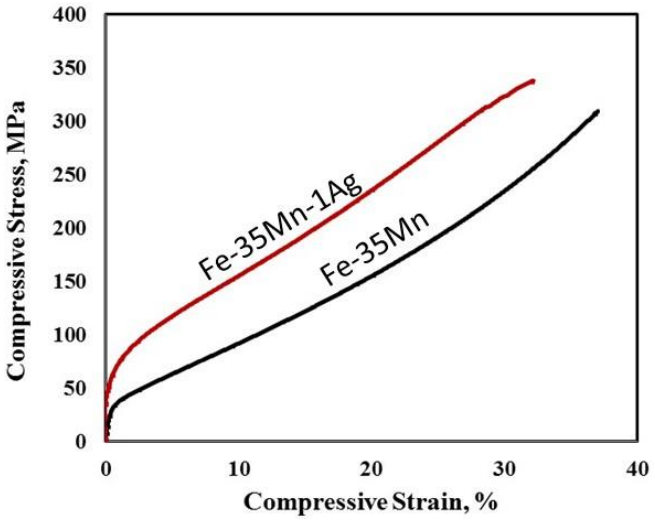

Figure 7 Typical compressive stress-strain curves of Fe-35Mn and Fe-35Mn-1Ag scaffolds

Table 2 Mechanical properties of Fe-35Mn and Fe-35Mn-1Ag scaffolds

Sample	σ0.2 (MPa)	σ30 (MPa)	Young's Modulus (GPa)
Fe-35Mn	41±2	235±5	14.76±2.50
Fe-35Mn-1Ag	75±4	324±7	14.59±2.65
Cortical Human Bone [59]	104-121	86-151	14-17

3-4) Degradation Behaviour

The 4-week immersion test in Hank's solution resulted in a corrosion rate of 0.122 ±0.05 mm/year and 0.161 ±0.07 mm/year for the SLM manufactured Fe-35Mn and Fe-35Mn-1Ag scaffold, respectively. As expected, addition of Ag to the Fe-Mn alloy increased the susceptibility of the scaffolds to galvanic corrosion. The noble Ag precipitates acted as

cathodes within the anodic Fe-Mn matrix, resulting in enhanced corrosion rate. These results are consistent with previously reported results (i.e. enhancement of degradation rate by addition of Ag to the Fe-Mn alloy system) by the current authors [5] as well as other researchers [33, 34, 67]. Tonna et al [68] also reported an increase in the corrosion current density of Fe-35Mn alloy by addition of 5.0 wt% Ag. However, there are some differences in the reported values since corrosion rate is significantly influenced by experimental methods and test parameters [46] as well as the specimen's manufacturing techniques. For instance, in the previous work the current authors [5] obtained a higher corrosion rate for Fe-35Mn and Fe-35Mn-1Ag alloys using a quasi-static flow test method [69], which is a more aggressive corrosive condition compared with the static immersion test method in the current work. The quasi-static flow test method is more suitable for testing medical devices that are implanted in organs where dynamic fluid movement conditions are existent, such as for stents that encounter flowing blood when implanted in a blood vessel. In contrast, the static immersion test is more suitable for conditions where fluid/material movement is minimal, such as for an orthopaedic scaffold implanted in the bone.

To evaluate the behaviour of material during the degradation process, the morphology, microstructure and elemental composition of samples surfaces after 28 days of immersion test were analysed using SEM and EDS. Figure 8 illustrates examples of SEM images and corresponding EDS maps from the matrix surface (Fig. 8b) and the internal surface of pores (Fig. 8c) of the Fe-35Mn-1Ag scaffolds.

The corrosion products formed on the surface of samples are different between scaffolds matrix (Figures 8b and d) and the inner porous surface (Figures 8c and e). On the surface of the matrix that was mechanically polished before immersion testing, a homogenous layer containing higher concentration of Ca, P and O was formed, indicative of calcium-phosphate product [22]. However, in this area some localised corrosion products highly contain Fe, Mn and O (arrows in Figure 8b) were also visible (Figure 8d) indicative of Fe-oxide and Mn-oxide products. As illustrated from EDS maps in Figure 8d, Fe and Mn also exist all over the surface of sample along with Ca, O and P, suggesting the presence of hydrated iron and Mn products [24, 34]. Previous study by the current authors [18] confirmed the presence of Fe and Mn hydroxides [$Fe(OH)_2$ and $Mn(OH)_2$] on the surface of Fe-35Mn alloy under similar immersion test. These hydroxide layers are the product of reactions between Fe and Mn ions (from oxidation reactions in Hank's solution) and hydroxyl ions, OH^-, (from the cathodic reaction) [22].

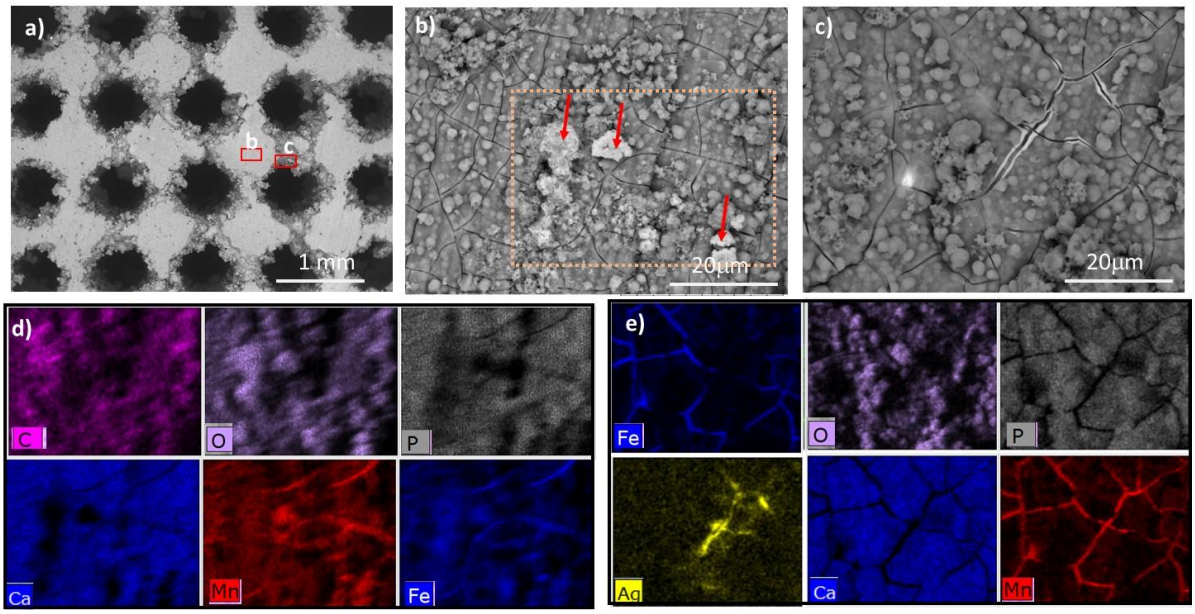

Figure 8 SEM micrograph of corrosion surfaces of Fe-35Mn-1Ag scaffolds. a) low magnification image, b) high magnification image of selected area from the polished matrix of the scaffold, c) high magnification image of selected area from internal pore surface of the scaffold, d) and e) represents EDS maps corresponding to surface areas in b) and c), respectively

As previously shown (Figure 3), the internal surface of the scaffolds has a higher surface area due to the presence of melt pool expansion and partially melted powders. An increase in the exposed surface area is expected to enhance the corrosion rate due to an increase in the probability of contact with corrosive elements (e.g. O_2 and H^+) [46]. Carluccio et al. [46] proposed that the bigger surface area within the porous structure of the scaffold could lead to the localized alkalization and formation of calcium-phosphates. Similar corrosion products are likely present in the inner surface of the pores, as indicated by the high concentrations of Ca and P in the EDS maps. Though the areas appear to be entirely depleted from Fe and Mn, a network of Fe and Mn is still visible in the cracked area of the corrosion product layer (Figure 8e). The detected Fe and Mn likely originates from the main scaffold that is present under the corrosion film. The presence of cracks in the corrosion product layer (calcium-phosphates) maybe beneficial for degradation. The crack network can allow the intrusion of corrosive fluids/material to the underlying metal surface, thereby promoting the continued degradation of the Fe-Mn alloy within the body environment.

Conclusions

Fe-35Mn and Fe-35Mn-1Ag highly porous scaffolds fabricated using selective laser melting process. The results can be summarised as follows:

- Scaffolds of Fe-35Mn and Fe-35Mn-1Ag with up to 60% lattice porosity and less than 1.4% processing porosities were successfully manufactured using pre-alloyed Fe-35Mn and elemental Ag powders.
- SLM manufactured scaffolds show sufficient geometrical fidelity with a limited number of pores and cracks in the matrix.

- Addition of 1.0 wt% silver to the Fe-35Mn alloy improved the mechanical properties and degradation behaviour of additively manufactured scaffolds.

- While addition of 1.0 wt% Ag increased the degradation rate of Fe-35Mn alloy by up to 30%, the compressive strength slightly increased with no significant influence on the modulus of elasticity.

- The overall mechanical properties and biodegradation behaviour of Fe-35Mn-1Ag alloy alongside with antibacterial effect of Ag, indelicate that alloy has high potential to be used as a biodegradable implant for load bearing applications.

- The results confirmed the suitability of this alloy for fabrication by SLM, providing opportunities for its use the manufacture and design of a range of components for different biomedical applications.

Acknowledgments

M. S. Dargusch acknowledges the support of the ARC Research Hub for Advanced Manufacturing of Medical Devices (IH150100024).

References

[1] Carluccio D, Demir A, Caprio L, Previtali B, Bermingham M, Dargusch M. The influence of laser processing parameters on the densification and surface morphology of pure Fe and Fe-35Mn scaffolds produced by selective laser melting. J Manuf. Process. 2019; 40: 113-121. https://doi.org/10.1016/j.jmapro.2019.03.018.
[2] Gao C, Yao M, Li S, Feng P, Peng S, Shuai C. Highly biodegradable and bioactive Fe-Pd-bredigite biocomposites prepared by selective laser melting. Journal of advanced research 2019; 20: 91-104. https://doi.org/10.1016/j.jare.2019.06.001.
[3] Zheng Y, Gu X, Witte F. Biodegradable metals. Mater. Sci. Eng., R 2014; 77: 1-34. https://doi.org/10.1016/j.mser.2014.01.001.
[4] Yusop A, Bakir A, Shaharom N, Abdul Kadir M, Hermawan H. Porous biodegradable metals for hard tissue scaffolds: a review. Inter. J Biomater. 2012; 2012: https://doi.org/10.1155/2012/641430.
[5] Dargusch MS, Venezuela J, Dehghan-Manshadi A, Johnston S, Yang N, Mardon K, Lau C, Allavena R. In Vivo Evaluation of Bioabsorbable Fe-35Mn-1Ag: First Reports on In Vivo Hydrogen Gas Evolution in Fe-Based Implants. Advanced Healthcare Materials 2020; 2000667. https://doi.org/10.1002/adhm.202000667.
[6] Prakasam M, Locs J, Salma-Ancane K, Loca D, Largeteau A, Berzina-Cimdina L. Biodegradable materials and metallic implants—a review. Journal of functional biomaterials 2017; 8: 44. https://doi.org/10.3390/jfb8040044.
[7] Niinomi M, Nakai M. Titanium-based biomaterials for preventing stress shielding between implant devices and bone. Inter. J Biomater. 2011; 2011: https://doi.org/10.1155/2011/836587.
[8] Okazaki Y, Gotoh E. Metal release from stainless steel, Co–Cr–Mo–Ni–Fe and Ni–Ti alloys in vascular implants. Corros Sci. 2008; 50: 3429-3438. https://doi.org/10.1016/j.corsci.2008.09.002.
[9] BIOTRONIK Announces CE Mark For Magmaris, The First Clinically-Proven Bioresorbable Magnesium Scaffold. in, https://www.meddeviceonline.com/doc/biotronik-announces-ce-mark-proven-magnesium-scaffold-0001, 2016.

[10] Zeng R, Dietzel W, Witte F, Hort N, Blawert C. Progress and challenge for magnesium alloys as biomaterials. Adv. Eng. Mater. 2008; 10: https://doi.org/10.1002/adem.200800035.
[11] Dehghan-Manshadi A, StJohn D, Dargusch M. Tensile Properties and Fracture Behaviour of Biodegradable Iron–Manganese Scaffolds Produced by Powder Sintering. Mater. 2019; 12: 1572. https://doi.org/10.3390/ma12101572.
[12] Gu X, Zheng Y, Cheng Y, Zhong S, Xi T. In vitro corrosion and biocompatibility of binary magnesium alloys. Biomater. 2009; 30: 484-498. https://doi.org/10.1016/j.biomaterials.2008.10.021.
[13] Song G. Control of biodegradation of biocompatable magnesium alloys. Corros Sci. 2007; 49: 1696-1701. https://doi.org/10.1016/j.corsci.2007.01.001.
[14] Witte F, Kaese V, Haferkamp H, Switzer E, Meyer-Lindenberg A, Wirth C, Windhagen H. In vivo corrosion of four magnesium alloys and the associated bone response. Biomater. 2005; 26: 3557-3563. https://doi.org/10.1016/j.biomaterials.2004.09.049.
[15] Chua K, Khan I, Malhotra R, Zhu D. Additive Manufacturing and 3D Printing of Metallic Biomaterials. Engineered Regeneration 2022; https://doi.org/10.1016/j.engreg.2021.11.002.
[16] Hufenbach J, Wendrock H, Kochta F, Kühn U, Gebert A. Novel biodegradable Fe-Mn-CS alloy with superior mechanical and corrosion properties. Mater. Lett. 2017; 186: 330-333. https://doi.org/10.1016/j.matlet.2016.10.037.
[17] Hermawan H, Dubé D, Mantovani D. Development of degradable Fe-35Mn alloy for biomedical application. in: Adv. Mater. Res., Trans Tech Publ; 2007, P. 107-112.
[18] Dargusch M, Dehghan-Manshadi A, Shahbazi M, Venezuela J, Tran X, Song J, Liu N, Xu C, Ye Q, Wen C. Exploring the role of manganese on the microstructure, mechanical properties, biodegradability and biocompatibility of porous iron-based scaffolds. ACS Biomaterials Science & Engineering 2019; https://doi.org/10.1021/acsbiomaterials.8b01497.
[19] Zhang Q, Cao P. Degradable porous Fe-35wt.% Mn produced via powder sintering from NH 4 HCO 3 porogen. Mater. Chem. Phys. 2015; 163: 394-401. https://doi.org/10.1016/j.matchemphys.2015.07.056.
[20] Liu B, Zheng Y. Effects of alloying elements (Mn, Co, Al, W, Sn, B, C and S) on biodegradability and in vitro biocompatibility of pure iron. Acta Biomater. 2011; 7: 1407-1420. https://doi.org/10.1016/j.actbio.2010.11.001.
[21] Hermawan H, Dubé D, Mantovani D. Degradable metallic biomaterials: design and development of Fe–Mn alloys for stents. J Biomed. Mater. Res. A 2010; 93: 1-11. https://doi.org/10.1002/jbm.a.32224.
[22] Hermawan H, Purnama A, Dube D, Couet J, Mantovani D. Fe–Mn alloys for metallic biodegradable stents: degradation and cell viability studies. Acta Biomater. 2010; 6: 1852-1860. https://doi.org/10.1016/j.actbio.2009.11.025.
[23] Schinhammer M, Hänzi AC, Löffler JF, Uggowitzer PJ. Design strategy for biodegradable Fe-based alloys for medical applications. Acta Biomater. 2010; 6: 1705-1713. https://doi.org/10.1016/j.actbio.2009.07.039.
[24] Čapek J, Kubásek J, Vojtěch D, Jablonská E, Lipov J, Ruml T. Microstructural, mechanical, corrosion and cytotoxicity characterization of the hot forged FeMn30 (wt.%) alloy. Mater. Sci. Eng. C 2016; 58: 900-908. https://doi.org/10.1016/j.msec.2015.09.049.
[25] Venezuela J, Dargusch M. Addressing the slow corrosion rate of biodegradable Fe-Mn: Current approaches and future trends. Current Opinion in Solid State and Materials Science 2020; 100822. https://doi.org/10.1016/j.cossms.2020.100822.
[26] Donik Č, Kraner J, Kocijan A, Paulin I, Godec M. Evolution of the ε and γ phases in biodegradable Fe–Mn alloys produced using laser powder-bed fusion. Scientific Reports 2021; 11: 1-10. https://doi.org/10.1038/s41598-021-99042-0.
[27] Fântânariu M, Trincă LC, Solcan C, Trofin A, Strungaru Ş, Şindilar EV, Plăvan G, Stanciu S. A new Fe–Mn–Si alloplastic biomaterial as bone grafting material: In vivo study. Applied Surface Science 2015; 352: 129-139. https://doi.org/10.1016/j.apsusc.2015.04.197.

[28] Liu B, Zheng Y, Ruan L. In vitro investigation of Fe30Mn6Si shape memory alloy as potential biodegradable metallic material. Mater. Lett. 2011; 65: 540-543. https://doi.org/10.1016/j.matlet.2010.10.068.
[29] Mandal S, Ummadi R, Bose M, Balla VK, Roy M. Fe–Mn–Cu alloy as biodegradable material with enhanced antimicrobial properties. Mater. Lett. 2019; 237: 323-327. https://doi.org/10.1016/j.matlet.2018.11.117.
[30] Cheng J, Zheng Y. In vitro study on newly designed biodegradable Fe-X composites (X= W, CNT) prepared by spark plasma sintering. J Biomed. Mater. Res. B 2013; 101: 485-497. https://doi.org/10.1002/jbm.b.32783.
[31] Schinhammer M, Pecnik CM, Rechberger F, Hänzi AC, Löffler JF, Uggowitzer PJ. Recrystallization behavior, microstructure evolution and mechanical properties of biodegradable Fe–Mn–C (–Pd) TWIP alloys. Acta Mater. 2012; 60: 2746-2756. https://doi.org/10.1016/j.actamat.2012.01.041.
[32] Huang T, Cheng J, Bian D, Zheng Y. Fe–Au and Fe–Ag composites as candidates for biodegradable stent materials. J Biomed. Mater. Res. B 2016; 104: 225-240. https://doi.org/10.1002/jbm.b.33389.
[33] Sotoudehbagha P, Sheibani S, Khakbiz M, Ebrahimi-Barough S, Hermawan H. Novel antibacterial biodegradable Fe-Mn-Ag alloys produced by mechanical alloying. Mater. Sci. Eng. C 2018; 88: 88-94. https://doi.org/10.1016/j.msec.2018.03.005.
[34] Liu R-Y, He R-G, Xu L-Q, Guo S-F. Design of Fe–Mn–Ag alloys as potential candidates for biodegradable metals. Acta Metallurgica Sinica (English Letters) 2018; 31: 584-590. https://doi.org/10.1007/s40195-018-0702-z.
[35] Huang C-C, Lam T-N, Amalia L, Chen K-H, Yang K-Y, Muslih MR, Singh SS, Tsai P-I, Lee Y-T, Jain J. Tailoring grain sizes of the biodegradable iron-based alloys by pre-additive manufacturing microalloying. Scientific reports 2021; 11: 1-12. https://doi.org/10.1038/s41598-021-89022-9.
[36] Shuai C, Li S, Peng S, Feng P, Lai Y, Gao C. Biodegradable metallic bone implants. Materials Chemistry Frontiers 2019; 3: 544-562. https://doi.org/10.1039/C8QM00507A
[37] Nie Y, Chen G, Peng H, Tang S, Zhou Z, Pei F, Shen B. In vitro and 48 weeks in vivo performances of 3D printed porous Fe-30Mn biodegradable scaffolds. Acta Biomater. 2021; 121: 724-740. https://doi.org/10.1016/j.actbio.2020.12.028.
[38] Arciola CR, Alvi F, An Y, Campoccia D, Montanaro L. Implant infection and infection resistant materials: a mini review. The International journal of artificial organs 2005; 28: 1119-1125. https://doi.org/10.1177/039139880502801109.
[39] Arjunan A, Robinson J, Al Ani E, Heaselgrave W, Baroutaji A, Wang C. Mechanical performance of additively manufactured pure silver antibacterial bone scaffolds. J Mech. Prop. Biomater. 2020; 112: 104090. https://doi.org/10.1016/j.jmbbm.2020.104090.
[40] Qing Y, Li K, Li D, Qin Y. Antibacterial effects of silver incorporated zeolite coatings on 3D printed porous stainless steels. Mater. Sci. Eng. C 2020; 108: 110430. https://doi.org/10.1016/j.msec.2019.110430.
[41] Shivaram A, Bose S, Bandyopadhyay A. Understanding long-term silver release from surface modified porous titanium implants. Acta Biomater. 2017; 58: 550-560. https://doi.org/10.1016/j.actbio.2017.05.048.
[42] Reyes-Jara A, Cordero N, Aguirre J, Troncoso M, Figueroa G. Antibacterial effect of copper on microorganisms isolated from bovine mastitis. Frontiers in microbiology 2016; 7: 626. https://doi.org/10.3389/fmicb.2016.00626.
[43] Jin G, Cao H, Qiao Y, Meng F, Zhu H, Liu X. Osteogenic activity and antibacterial effect of zinc ion implanted titanium. Colloids and Surfaces B: Biointerfaces 2014; 117: 158-165. https://doi.org/10.1016/j.colsurfb.2014.02.025.
[44] Rizzello L, Pompa PP. Nanosilver-based antibacterial drugs and devices: mechanisms, methodological drawbacks, and guidelines. Chemical Society Reviews 2014; 43: 1501-1518. https://doi.org/10.1039/C3CS60218D

[45] Dehghan-Manshadi A, Chen Y, Shi Z, Bermingham M, StJohn D, Dargusch M, Qian M. Porous Titanium Scaffolds Fabricated by Metal Injection Moulding for Biomedical Applications. Mater. 2018; 11: 1573. https://doi.org/10.3390/ma11091573.
[46] Carluccio D, Xu C, Venezuela J, Cao Y, Kent D, Bermingham M, Demir AG, Previtali B, Ye Q, Dargusch M. Additively manufactured iron-manganese for biodegradable porous load-bearing bone scaffold applications. Acta Biomater. 2020; 103: 346-360. https://doi.org/10.1016/j.actbio.2019.12.018.
[47] Carluccio D, Demir A, Bermingham M, Dargusch M. Challenges and opportunities in the selective laser melting of biodegradable metals for load-bearing bone scaffold applications. Matall. Mater. Trans. A. 2020; 51: 3311-3334. https://doi.org/10.1007/s11661-020-05796-z.
[48] Maietta S, Gloria A, Improta G, Richetta M, De Santis R, Martorelli M. A further analysis on Ti6Al4V lattice structures manufactured by selective laser melting. Journal of healthcare engineering 2019; 2019: https://doi.org/10.1155/2019/3212594.
[49] Levy GN, Schindel R, Kruth J-P. Rapid manufacturing and rapid tooling with layer manufacturing (LM) technologies, state of the art and future perspectives. CIRP annals 2003; 52: 589-609. https://doi.org/10.1016/S0007-8506(07)60206-6.
[50] Carluccio D, Bermingham M, Kent D, Demir AG, Previtali B, Dargusch MS. Comparative study of pure iron manufactured by selective laser melting, laser metal deposition, and casting processes. Adv. Eng. Mater. 2019; 21: 1900049. https://doi.org/10.1002/adem.201900049.
[51] Demir AG, Previtali B. Multi-material selective laser melting of Fe/Al-12Si components. Manufacturing letters 2017; 11: 8-11.
[52] Lv Y, Wang B, Liu G, Tang Y, Lu E, Xie K, Lan C, Liu J, Qin Z, Wang L. Metal material, properties and design methods of porous biomedical scaffolds for additive manufacturing: A review. Frontiers in Bioengineering and Biotechnology 2021; 9: 194. https://doi.org/10.3389/fbioe.2021.641130.
[53] Xiong W, Hao L, Li Y, Tang D, Cui Q, Feng Z, Yan C. Effect of selective laser melting parameters on morphology, microstructure, densification and mechanical properties of supersaturated silver alloy. Mater. Design. 2019; 170: 107697. https://doi.org/10.1016/j.matdes.2019.107697.
[54] Rajagopalan S, Robb RA. Schwarz meets Schwann: design and fabrication of biomorphic and durataxic tissue engineering scaffolds. Medical image analysis 2006; 10: 693-712. https://doi.org/10.1016/j.media.2006.06.001.
[55] Johnson PB, Christy R-W. Optical constants of the noble metals. Physical review B 1972; 6: 4370. https://doi.org/10.1103/PhysRevB.6.4370.
[56] Johnson P, Christy R. Optical constants of transition metals: Ti, v, cr, mn, fe, co, ni, and pd. Physical review B 1974; 9: 5056. https://doi.org/10.1103/PhysRevB.9.5056.
[57] Carluccio D, Bermingham M, Dargusch M, Demir AG, Caprio L, Previtali B. Selective laser melting Fe and Fe-35Mn for biodegradable implants. International Journal of Modern Physics B 2020; 34: 2040034. https://doi.org/10.1142/S0217979220400342.
[58] Soro N, Attar H, Wu X, Dargusch MS. Investigation of the structure and mechanical properties of additively manufactured Ti-6Al-4V biomedical scaffolds designed with a Schwartz primitive unit-cell. Mater. Sci. Eng. A 2019; 745: 195-202. https://doi.org/10.1016/j.msea.2018.12.104.
[59] Wang X, Xu S, Zhou S, Xu W, Leary M, Choong P, Qian M, Brandt M, Xie YM. Topological design and additive manufacturing of porous metals for bone scaffolds and orthopaedic implants: A review. Biomater. 2016; 83: 127-141. https://doi.org/10.1016/j.biomaterials.2016.01.012.
[60] Calignano F. Design optimization of supports for overhanging structures in aluminum and titanium alloys by selective laser melting. Mater. Design. 2014; 64: 203-213. https://doi.org/10.1016/j.matdes.2014.07.043.
[61] Anilli M, Demir AG, Previtali B. Additive manufacturing of laser cutting nozzles by SLM: processing, finishing and functional characterization. Rapid Prototyping Journal 2018; https://doi.org/10.1108/RPJ-05-2017-0106.

[62] Kruth J-P, Badrossamay M, Yasa E, Deckers J, Thijs L, Van Humbeeck J. Part and material properties in selective laser melting of metals. in: Proceedings of the 16th International Symposium on Electromachining (ISEM XVI), SHANGHAI JIAO TONG UNIV PRESS, 2010, pp. 3-14.
[63] Galy C, Le Guen E, Lacoste E, Arvieu C. Main defects observed in aluminum alloy parts produced by SLM: from causes to consequences. Additive manufacturing 2018; 22: 165-175. https://doi.org/10.1016/j.addma.2018.05.005.
[64] Yakout M, Elbestawi M, Veldhuis SC. Density and mechanical properties in selective laser melting of Invar 36 and stainless steel 316L. J Mater. Proc. Technol. 2019; 266: 397-420. https://doi.org/10.1016/j.jmatprotec.2018.11.006.
[65] Martínez J, Cotes S, Cabrera A, Desimoni J, Guillermet AF. On the relative fraction of ε martensite in γ-Fe–Mn alloys. Mater. Sci. Eng. A 2005; 408: 26-32. https://doi.org/10.1016/j.msea.2005.06.019.
[66] Reilly DT, Burstein AH. The mechanical properties of cortical bone. JBJS 1974; 56: 1001-1022.
[67] Wiesener M, Peters K, Taube A, Keller A, Hoyer KP, Niendorf T, Grundmeier G. Corrosion properties of bioresorbable FeMn-Ag alloys prepared by selective laser melting. Materials and Corrosion 2017; 68: 1028-1036. https://doi.org/10.1002/maco.201709478.
[68] Tonna C, Wang C, Mei D, Lamaka SV, Zheludkevich ML, Buhagiar J. Biodegradation behaviour of Fe-based alloys in Hanks' Balanced Salt Solutions: Part I. material characterisation and corrosion testing. Bioactive materials 2022; 7: 426-440. https://doi.org/10.1016/j.bioactmat.2021.05.048.
[69] Johnston S, Shi Z, Atrens A. The influence of pH on the corrosion rate of high-purity Mg, AZ91 and ZE41 in bicarbonate buffered Hanks' solution. Corros Sci. 2015; 101: 182-192. https://doi.org/10.1016/j.corsci.2015.09.018.